

Article

Distribution, Transport, and Impact on Air Quality of Two Typical Dust Events in China in 2021

Qia Ye and Xiaoshen Zheng *

College of Marine and Environmental Sciences, Tianjin University of Science and Technology, Tianjin 300457, China
* Correspondence: zxs@tust.edu.cn

Abstract: The dust event from 12 January to 17 January 2021 (“1.12 event”) is the first dust process in 2021 and the earliest dust event in the last two decades. The dust event from 14 to 18 March 2021 (“3.15 event”) was the strongest dust storm in the past decade. Distribution, transport, and impact on urban air quality of these two typical dust events were studied using multi-source satellite data, a HYSPLIT trajectory model, and a 3D concentration-weighted trajectory model. Results show that both dust events affected a wide range of areas, covering Northwest, North, Northeast, East, and Central-South China. A strong dust belt spanning Northwest, North, and Northeast China was formed in northern China on 15 March 2021. The distribution heights of the 1.12 and 3.15 events were 0–5 km and 0–10 km, respectively. Dust from western Inner Mongolia and southern Mongolia dominated the 1.12 event, while dust from southern Mongolia dominated the 3.15 event. Both of these dust sources had eastward and southeastward transport paths. The majority of the dust was near-ground in downstream cities from an altitude of 0–3 km. Most cities were affected by the dust backflow. The 1.12 event generated more severe particulate pollution in southern China than the 3.15 event. During high-value dust days, ozone pollution levels decreased at the majority of stations. Dust weather with low dust rising heights and dust backflow phenomena should be taken seriously in urban dust pollution forecasting and warning work. International collaboration is needed to improve China’s desertification control.

Keywords: atmospheric remote sensing; dust storm; dust pollution; 3D-CWT



Citation: Ye, Q.; Zheng, X.

Distribution, Transport, and Impact on Air Quality of Two Typical Dust Events in China in 2021. *Atmosphere* **2023**, *14*, 432. <https://doi.org/10.3390/atmos14030432>

Academic Editors: Ana Vukovic and Slobodan Nickovic

Received: 16 January 2023

Revised: 15 February 2023

Accepted: 17 February 2023

Published: 21 February 2023



Copyright: © 2023 by the authors. Licensee MDPI, Basel, Switzerland. This article is an open access article distributed under the terms and conditions of the Creative Commons Attribution (CC BY) license (<https://creativecommons.org/licenses/by/4.0/>).

1. Introduction

Dust particles constitute more than half of total tropospheric aerosols [1], having an influence on the regional and global atmospheric environment. They may directly impact the earth-atmosphere system’s radiative transmission by absorbing and reflecting solar and long-wave radiation [2,3], as well as act as cloud condensation nuclei and ice nuclei to change cloud microphysical characteristics and alter precipitation [4,5]. Meanwhile, dust aerosols are the main natural source of urban particulate pollution [6,7]. Particles carried by dust can enter the lungs and blood through the respiratory tract, which can be a serious hazard to human health, for example in the respiratory and cardiovascular systems [8–10]. Dust can be transported by weather systems, causing varying degrees of atmospheric pollution in the dust source area and downstream cities along the transport path [11–13]. The mixture of foreign dust and local urban anthropogenic pollutants can further aggravate air pollution through chemical reactions and meteorological feedback [10]. Therefore, understanding the distribution and transport characteristics of dust activities, as well as the impact of dust on urban air quality, is critical to urban air environment management and human health.

China’s desertification area is vast, accounting for 27% of the total national territory [14]. The Taklamakan Desert in Xinjiang, China, and the Gobi Desert on the border of Northwest China and southern Mongolia are the principal dust sources in East Asia [15]. Their annual emissions account for around 10–25% of total global dust emissions [16]. As a

result, Northwest China is prone to dusty days and dust storms [17]. Notably, a growing number of studies show that urban particulate matter concentrations in non-sand-source areas, such as the central and southern regions of China, are also affected by large amounts of dust, frequent combined pollution by dust and man-made pollution due to the long-range transport nature of dust [6,18]. Statistics show that between 2015 and 2020, dust incidents occurred in 334 Chinese cities, excluding Shenzhen and Dongguan [19]. Polluted dust accounts for approximately 45% of the aerosols below 1.8 km in northern China [20]. The impact of dust events on non-sand-source cities in China has not been adequately studied.

In addition to particle matter, ozone is a prominent form of urban air pollution in China [21,22]. O₃ concentrations in Chinese cities have increased from 2015 to 2019 [23]. The frequency of ozone pollution events in megacities such as Beijing-Tianjin-Hebei, the Yangtze River Delta, and the Pearl River Delta are significantly higher than those in other regions [24]. Ozone pollution has emerged as a key concern for improving urban air quality in China [25]. Some studies have shown that dust and ozone have complex interactions [26]. Nevertheless, there are relatively few studies on the changes of urban ozone pollution during dust events [27]. With the Mongolian plateau undergoing a heat wave and drought cycle [28] and the increasing trend of wind speed in the sand source area [29], dust weather in East Asia may become more common and longer lasting [30] in the future. Therefore, the negative consequences of dust events on urban air quality in China cannot be ignored. The dusty weather from 12 January to 17 January 2021 (1.12 event), was China's first dust event in 2021 [31], occurring more than 30 days earlier than the average time of the first dust event from 2000 to 2020. The intense dust storm of 14–18 March 2021 (3.15 event) was China's most vigorous dust process in the previous decade, affecting nearly half of the country's territory [32]. Wang et al. (2022) analyzed atmospheric circulation conditions and dust distribution during the 1.12 event using multi-source remote sensing data. Runchuan (2022) used radionuclides to pinpoint the sources of dustfall in seven northern cities during the 3.15 event. Many academics have used synoptic analysis and physical quantity diagnosis to investigate the cause of the 3.15 dust storm [33,34]. Particle pollution in northern Chinese cities due to the 3.15 dust storm has also been discussed [32,35]. Most research, however, has concentrated on the meteorological causes of these two dust processes, in addition to the dust pollution experienced by cities near sand source areas [18,36]. The dust source pathways in non-sand-source regions such as South-Central China and East China and the dust pollution in southern China have been rarely discussed.

This paper began with a detailed examination of the spatial and temporal distribution of these two dust events using satellite data, ground station data, and reanalysis data. Combining the HYSPLIT model and the 3D-CWT model, this paper investigates the origin and transport characteristics of these dust events, resolves the regional differences in pollution caused by these two dust events, and illustrates the importance of dust height in influencing downstream urban particulate matter concentrations. Finally, the changes in urban particulate matter and ozone pollution during these two dust processes were explored using data from ground-based air quality monitoring stations. The purpose of this study is to provide scientific references for early warning of urban dust pollution as well as vital data for research on the environmental effects of dust aerosols.

2. Study Area, Data, and Methods

2.1. Study Area

The largest dust source areas in East Asia are the arid and semi-arid regions of Mongolia and northern China, dominated by the Taklamakan and Gobi deserts. With high emissions and an extensive area, the East Asian dust source is the second largest dust source region after the Sahara, accounting for about 10–25% of total global dust emissions each year [37,38]. Northern China is an important part of the dust sources in East Asia, where the exposed surface and abundant loose material, coupled with frequent high winds, make it easy to raise dust [39]. Mongolia, which borders northern China, has a continental semi-arid climate and is experiencing severe desertification as a result of global warming

and human activities [29]. From January to March 2021, the northern parts of China and Mongolia showed a weather situation with significantly higher temperatures and less precipitation [40,41]. In this context, the early thawing and loose surface layer of soils in the north of China and Mongolia are very favorable to surface dust raising [29]. Figure 1 depicts the distribution of each type of sand as well as China's six geographical divisions: Northeast, Northwest, Southwest, North, Central-South, and East China. The study area is north of 25° N in China. In this paper, we refer to the area south of 35° N as the southern region for purposes of description.

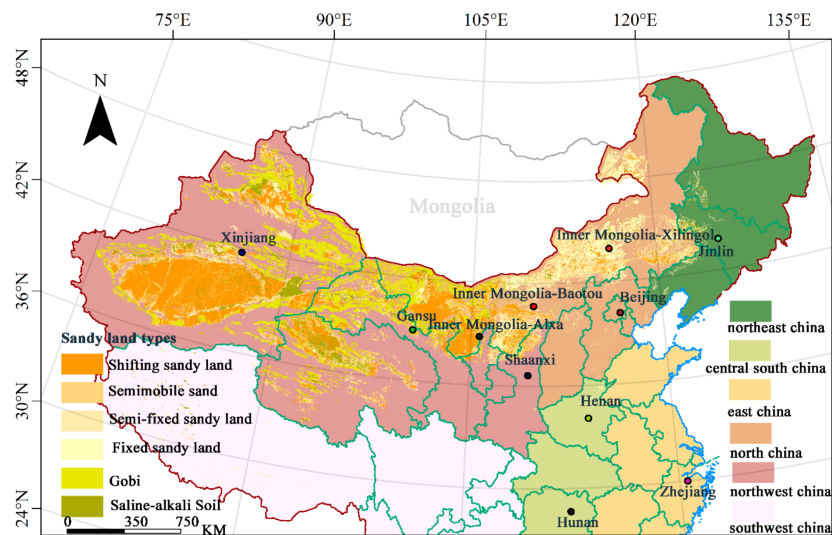


Figure 1. Geographical zoning and sand distribution in the study area.

2.2. Satellite Data

Satellite remote sensing has evolved into a powerful tool for the dynamic monitoring of widespread dust events. Sentinel-5P is a solar-synchronous polar orbiting satellite launched by the European Space Agency in 2017 that allows for global observations in a single day. It is equipped with the Tropospheric Monitoring Instrument (TROPOMI), which has the highest spatial resolution of any atmospheric monitoring spectrometer [42]. TROPOMI provides a UV-absorbing Aerosols Index (UVAI) product that can characterize the content of ultraviolet absorbing aerosols such as dust and smoke through UV channel inversion parameters [43]. If absorbing aerosols are present in the atmosphere, the UVAI is greater than 0, and the absorbing intensity is proportional to the UVAI value. This is the formula for UVAI [44]:

$$UVAI = -100 \log_{10} \left(\frac{I_{354}^{obs}}{I_{354}^{cal}} \right) \quad (1)$$

where I_{354}^{obs} and I_{354}^{cal} represent the actual radiation intensity observed by the satellite sensor and the calculated value of the radiative transfer model, respectively.

We used UVAI data to obtain the daily horizontal distribution of dust events. Because TROPOMI could not cover all of China in a single observation, the UVAI images of the entire day were stitched together by taking the maximum value of image elements at the image overlap. The data were obtained from the Sentinel-5P official website (<https://s5phub.copernicus.eu/dhus/#/home> (accessed on 14 November 2021)), with a bandwidth of 2600 km and a spatial resolution of 7 km × 3.5 km. Credible data with QA values greater than 0.5 were screened based on the satellite product's official recommendations.

The Cloud-Aerosol Lidar and Infrared Pathfinder Satellite Observation (CALIPSO) satellite, launched in 2006, carries the Cloud-Aerosol Lidar with Orthogonal Polarization (CALIOP), the most widely used satellite-based lidar today [45]. CALIOP's Vertical Feature Mask (VFM) can identify aerosol types by inverting the optical properties of aerosols [46].

The vertical distribution of each type of aerosol during dust events was determined using CALIOP's VFM product in this study. The data were downloaded from the NASA website (<https://search.earthdata.nasa.gov> (accessed on 20 November 2021)). The temporal resolution is 15 min, and the vertical resolution varies with altitude: 30 m (−500 m–8.2 km), and 60 m (8.2–20.2 km). The data were screened using the quality control parameters of the VFM product as criteria, with feature type QA not equal to 0 and subtype QA not equal to 0.

2.3. MERRA-2 Dust Mixing Ratio

MERRA-2 is the most recent version of satellite-era global atmospheric reanalysis data produced by NASA's Global Modeling and Assimilation Office (GMAO) using the Goddard Earth Observing System Model (GEOS) and has a higher accuracy compared to the MERRA dataset [47]. Yao et al. (2020)'s research demonstrated that MERRA-2 model representations of dust events in East Asia are generally consistent with ground and satellite observations. In order to analyze the evolution of the distribution height of dust events, daily averages of the sum of dust aerosol mixing ratios for six different effective radius datasets (bin-001, 0–0.73 μm ; bin-002, 0.73–1.4 μm ; bin-003, 1.4–2.4 μm ; bin-004, 2.4–4.5 μm ; bin-005, 4.5–8.0 μm ; bin-all, 0–8.0 μm) were calculated. The data were obtained by visiting <https://gmao.gsfc.nasa.gov/reanalysis/MERRA-2/> (accessed on 30 June 2022). MERRA-2 has a spatial resolution of $0.625^\circ \times 0.5^\circ$ and a temporal resolution of 1 h.

2.4. Ground Station Data

The China Real-Time Urban Air Quality Release Platform (<http://106.37.208.233:20035> (accessed on 1 June 2022)) provides air pollutant data from automatic air quality monitoring stations in China hour by hour. We chose 11 ground stations (Figure 1) and compared the effects of the two dust processes on urban air quality using hourly data from their PM_{10} , $\text{PM}_{2.5}$, and ozone concentrations.

2.5. HYSPLIT Model

The Hybrid Single-Particle Lagrangian Integrated Trajectory (HYSPLIT) model is a professional model developed by the National Oceanic and Atmospheric Administration and the Australian Bureau of Meteorology to simulate and calculate dispersion trajectories [48]. It uses the Lagrangian method to calculate the trajectories of air masses and simulate complex particle diffusion and sedimentation processes, and has been widely used in the study of the transport and dispersion of various pollutants [49,50].

In order to explore the transport path of dust, we simulated the forward trajectory of air masses at the dust source and the backward trajectory of air masses at the cities downstream of dust transport using the HYSPLIT model. According to the principle that the total spatial variation (TSV) is significantly increasing, the angular distance clustering method is used to cluster the trajectories of air masses. The initial meteorological field for the HYSPLIT model is hourly meteorological element data from the Global Data Assimilation System of the National Centers for Environmental Prediction with a spatial resolution of $0.5^\circ \times 0.5^\circ$ and a temporal resolution of 6 h.

2.6. The Structure of 3D-CWT Model

The concentration-weighted trajectory (CWT) model is a widely used tool [51–53] that combines air mass trajectories and pollutant concentrations to effectively localize the source of pollutants. This model extends the traditional two-dimensional method by screening trajectories for different height layers [54]. It allows for the differentiation of pollutant source heights.

The 3D-CWT model is based on the following equation:

$$3D - C_{ijh} = \frac{\sum_{k=1}^v C_k \cdot t_{ijkh}}{\sum_{k=1}^v t_{ijkh}} = \frac{\sum_{k=1}^v C_k \cdot t_{ijkh}}{t_{ijh}} \quad (2)$$

$3D - C_{ijh}$ reflects the average weighted concentration of pollutants at the receptor point as the air mass passes through the grid ij within the h height layer. C_k is the pollutant concentration at the receptor point when trajectory k passes through grid ij . t_{ijkh} is the number of trajectory points belonging to trajectory k in grid cell ij of layer h . t_{ijh} is all the trajectory points in the h layer's grid cell ij .

To lessen the mistakes brought on by the insufficient number of trajectory points, the weight function $3D - W_{ijh}$ is added and multiplied by $3D - C_{ijh}$:

$$3D - W_{ijh} = \begin{cases} 1.0 & (3t_{ave,h} \leq t_{ijh}) \\ 0.7 & (1.5t_{ave,h} \leq t_{ijh} < 3t_{ave,h}) \\ 0.4 & (t_{ave,h} \leq t_{ijh} < 1.5t_{ave,h}) \\ 0.2 & (t_{ijh} < t_{ave,h}) \end{cases} \quad (3)$$

where $t_{ave,h}$ is the total number of trajectory points divided by the total number of grids.

An improved 3D-CWT model has been successfully used to investigate the geographical origin and transported altitudinal layers of pollutants such as water soluble ions in $PM_{2.5}$ [55], PM_{10} , and PM_1 chemical composition [56], as well as atmospheric polycyclic aromatic hydrocarbons [54]. This paper divides dust heights into four height layers based on satellite and reanalysis data: 0–500 m, 500–1500 m, 1500–3000 m, and more. In this study, we divided the study area into a $1^\circ \times 1^\circ$ horizontal grid. Combining the air mass trajectory points calculated from the HYSPLIT model and PM_{10} data from ground stations, the 3D-CWT model was used to calculate the potential source of surface dust characterized by PM_{10} in downstream cities within these four different height layers. This study is the first to analyze dust source pathways using the 3D-CWT model, increasing the application of the 3D-CWT model in determining the sources of atmospheric pollutants.

3. Results and Discussion

3.1. Spatial-Temporal Distribution of Dust Events

Positive values of TROPOMI UVAI can indicate the presence of absorbing aerosols, such as dust, black carbon, and organic carbon. Black carbon and organic carbon aerosols mainly originate from biomass burning [43]. Since there were few large-scale biomass burning events, such as crop straw burning and forest fires, in China in January and March of the study year, the absorbing aerosols indicated by positive UVAI values in Figure 2 should be not black carbon aerosols but raised dust aerosols. It can be seen that in the 1.12 event, the dust appeared first in western Inner Mongolia. Then, from the 13th to the 14th, it spread eastward to appear over North and Northeast China. On the 15th to 16th, the dust aerosols moved southward and were observed in the northern part of the Central-South China. The values of UVAI are mainly in the range of 0 to 1, which indicates the relatively low intensity of this dust event.

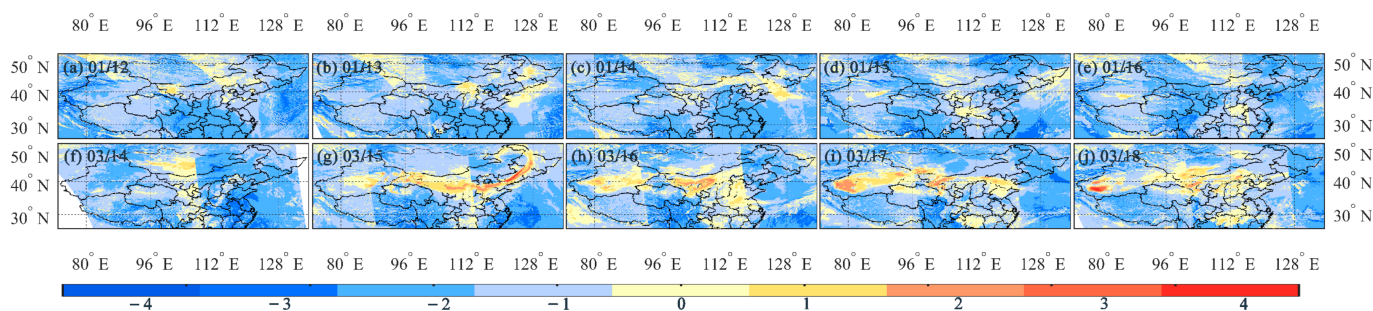


Figure 2. Horizontal distribution of dust in the 1.12 and 3.15 events, indicated by TROPOMI UVAI.

The high UVAI values (0–4) from 14–18 March demonstrated the high dust intensity of the 3.15 event. On 14 March, extensive and intense dust was monitored over the Gobi Desert in southern Mongolia. Then on 15 March, a high-intensity dust band (UVAI > 2) appeared across northern China between 38°–42° N and 80°–128° E. From the 17th to the 18th, the intensity of the sand and dust in western Inner Mongolia continued to decline. The dust-affected area expanded southward to the southern parts of northern China, South-Central China, and eastern China. These two sand and dust events are characterized by wide coverage. Northwest, North, Northeast, South-Central and East China were all affected. Furthermore, the intensity of the 3.15 event and its dust storm range were significantly higher than those of the 1.12 event.

Constrained by observational time and inversion algorithms, satellites will inevitably miss the monitoring of dust aerosols. As the main component of dust aerosols, PM₁₀ is often used to characterize near-surface dust concentrations during dust events [57–59]. To obtain a more comprehensive range of dust, we selected 11 ground stations evenly distributed in the study area and used their daily averages of PM₁₀ concentrations to complement the information provided by UVAI on the location and intensity of dust. Five of these stations, Xinjiang, Gansu, Alxa, Baotou, and Xinlingol, are located near the dust source, while six stations, Jinlin, Beijing, Shaanxi, Henan, Hunan, and Zhejiang, are located in cities downstream of the dust source.

As shown in Figure 3, during the 1.12 event, the daily average PM₁₀ values in Alxa and Baotou in western Inner Mongolia gradually increased from the 10th January to the 13th January, reaching peak values of 1450 and 1230 µg/m³, respectively. After that, they gradually decreased. Xilingol station in central Inner Mongolia, on the other hand, showed consistently lower PM₁₀ concentrations. Gansu and Xinjiang stations exhibited relatively flat changes in PM₁₀ values. This indicates that the extent of the strong sand and dust in this event were mainly concentrated in western Inner Mongolia. PM₁₀ peaks at the Jilin, Beijing, and Henan sites occurred from the 13th to the 15th, and those of the Hunan and Zhejiang sites occurred from the 15th to the 16th. This is consistent with the information shown by TROPOMI UVAI that dust moved eastward, first from western Inner Mongolia, and then spread southward. Meanwhile, PM₁₀ data from the Hunan and Zhejiang stations supplemented UVAI's missing information on dust over Central-South and East China.

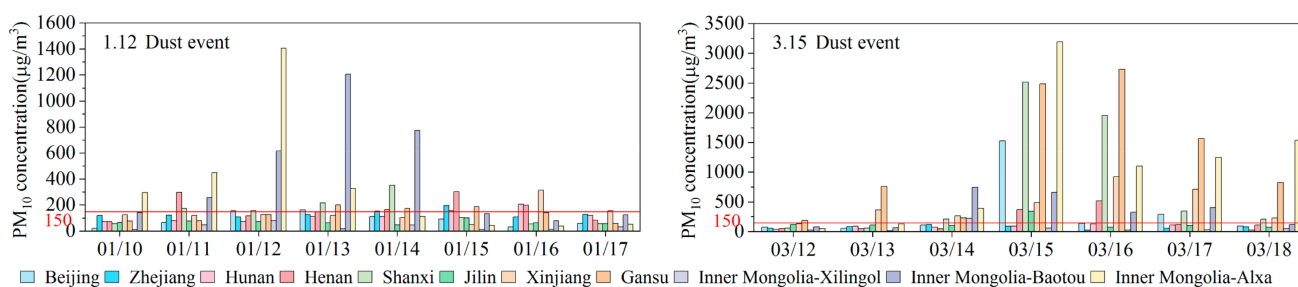


Figure 3. Daily average PM₁₀ values at ground stations during the 1.12 and 3.15 events.

On March 12 to 18, ground station PM₁₀ values fully reflected the high intensity of the 3.15 dust storm. It can be seen that on 14 March, the Baotou site in central and western Inner Mongolia had a daily average PM₁₀ value as high as 830 µg/m³. On March 15, the Alxa, Gansu, Shaanxi, Beijing, and Jilin sites had ultra-high PM₁₀ peaks of 3190, 2483, 2511, 1524, and 338 µg/m³, respectively. This is consistent with the extent of the strong dust belt in the north indicated by TROPOMI UVAI. After that, the PM₁₀ values at each site gradually decreased, with only the Gansu and Alashan sites in western Inner Mongolia having persistently high values. This also matches the evolutionary characteristics of the strong dust range shrinking to the west. It is worth noting that although UVAI shows that there is a wide range of sand and dust over South-Central and East China from 16 to 18, there is no correspondingly large change in PM₁₀ values of the Hunan and Zhejiang sites. As the satellite products detect the content of dust in the whole atmosphere, the PM₁₀ data

from ground stations indicate the dust concentration near the ground, from which it can be reasonably assumed that the dust over South-Central and East China was distributed at a high altitude and had not yet settled to the ground. Since the Xinjiang site is at the northern edge of the Taklamakan Desert, it cannot indicate the intensity of dust events in the desert hinterland and did not exhibit the ultra-high PM₁₀ corresponding to the strong dust shown by UVAI. This also illustrates the necessity and advantage of using satellites to monitor dust events.

To explore the vertical height characteristics of these two dust events, dust aerosol mixing ratio data from MERRA-2 (Figures 4 and 5) and CALIPSO VFM (Figure 6) were combined for analysis. It can be observed from Figure 4 that from the 12th to the 14th of January, dust gradually lifted during the transport from western Inner Mongolia to the east. On the 15th, part of the dust reached a height of 5 km in northern China. From January 16 to 17, dust gradually settled during delivery to South-Central China, and its height decreased from 5 km to 1.5 km.

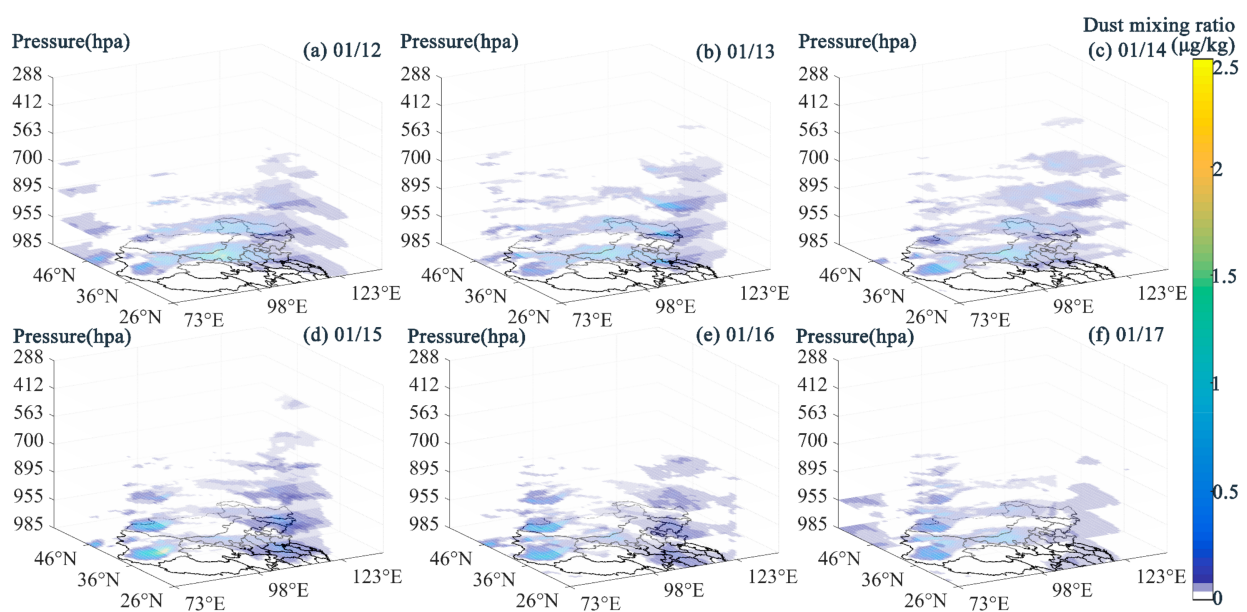


Figure 4. MERRA-2 dust mixing ratio during the 1.12 event.

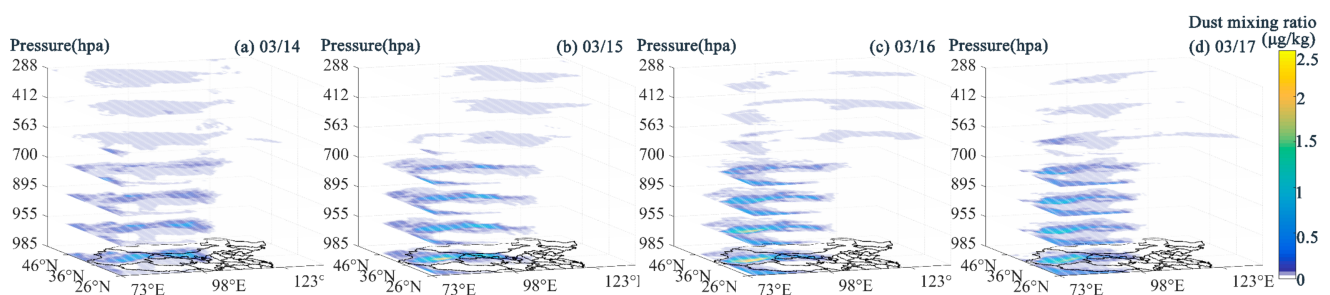


Figure 5. MERRA-2 dust mixing ratio during the 3.15 event.

The 3.15 event had a significantly greater dust altitude than 1.12. On 14 March, the dust layer in southern Mongolia and western Inner Mongolia reached 10 km or higher. It was followed by a significant southward movement of dust above 5 km. The Taklamakan Desert produced a large amount of surface dust from the 15th to the 16th, reaching heights of 5 km. However, for downstream cities, MERRA-2 only detected a small amount of dust distributed over 5–10 km in South-Central and East China.

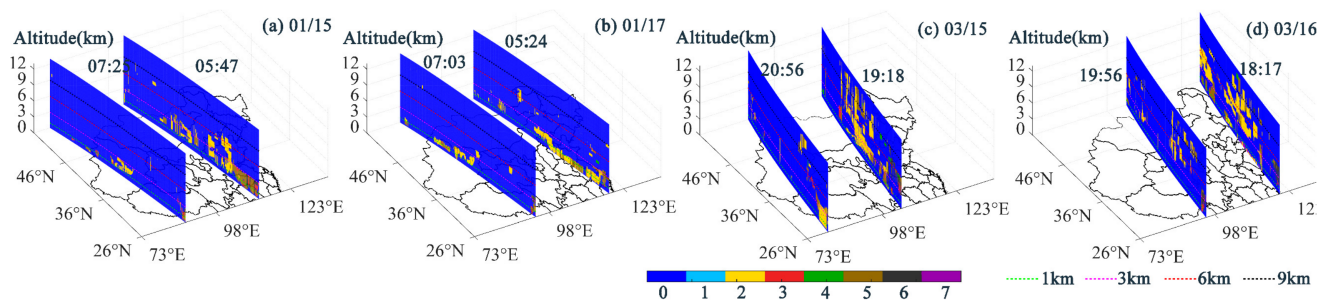


Figure 6. CALIOP VFM images on January 13 (a), January 15 (b), March 15 (c), and March 16 (d). (0 = Not Determined, 1 = Clean Marine, 2 = Dust, 3 = Polluted Continental/Smoke, 4 = Clean Continental, 5 = Polluted Dust, 6 = Elevated Smoke, 7 = Dusty Marine).

CALIOP VFM provides the vertical distribution of atmospheric aerosols. VFM images for 15 January, 16 January, 15 March, and 16 March were selected (Figure 6). The figure shows that dust in South-Central China reached an altitude of 5 km on 15 January and settled to 1.5 km on January 17. And dust over southern Mongolia, central Inner Mongolia, and northeastern China was found at altitudes of 1 to 10 km on 15 and 17 March. The above analysis shows that the dust heights monitored by CALIPSO VFM are consistent with those of MERRA-2, and the overall description of dust heights by the MERRA-2 product is not greatly erroneous. Meanwhile, combining the MERRA-2 and VFM images on 16 and 17 March, we can see that the dust in South-Central and East China was indeed distributed at altitudes above 3 km. This supports our previous speculation that the dust did not settle to the ground in South-Central and East China on 16 and 18 March by comparing UVAI and PM_{10} data.

In addition, it can be observed through VFM that the main aerosol types over the southern areas on 15 and 17 January were polluted dust. This should be related to dust transport height. Before the 15th, the dust transmission height was relatively low, making it more likely to mix with anthropogenic pollutants on the ground, resulting in polluted dust. The dust on the 17th should be the deposition of high-altitude dust, so there was less mixing with anthropogenic pollutants. Overall, in the 1.12 event, the dust first rose and then settled, with the main distribution height between 0 and 5 km. In the 3.15 event, the dust rose at a high altitude at the beginning, and then it gradually settled. Its main distribution height was 0–10 km. The transmission height of dust affects its aerosol type.

3.2. Dust Transport Paths

The analysis of satellite and ground stations as well as reanalysis data shows that the two dust events impacted the majority of China's cities. However, due to the observed data's limited spatiotemporal resolution, it is impossible to track the dust transport path dynamically. Therefore, simulation points are set up based on the characteristics of dust locations obtained from multi-source observation data. The HYSPLIT trajectory model and the 3D-CWT method are used to simulate the outward dust transport from the sand source as well as the dust input paths over the downstream cities.

After analyzing the spatial-temporal distribution of dust events, it was discovered that the main sand source areas were southern Mongolia, western Inner Mongolia, and central Xinjiang, and that the main dust rise periods were 12–14 January and 14–16 March. As shown in Figure 7, the forward 500 m trajectories of the three dust source areas were simulated and clustered. To provide a clearer introduction to dust transportation, we discuss the dust tracks in conjunction with other scholars' findings on the weather situation during these two dust events.

On 12 January, gusty winds with gusts up to 18 m/s blew southeasterly in western Inner Mongolia and southern Mongolia, influenced by unusual cyclonic circulation [60]. The gales carried dust to North China at a height of 1–2 km. On the 13th, cold cyclones in the mid-latitudes moved southeastward [40]. Dust from central and western Inner Mongolia was transported east and southeast at a height of more than 2 km, affecting

eastern Inner Mongolia, northeastern China, northern China, and southeastern Northwest China. The dust in southern Mongolia and western Inner Mongolia moved southeastward on the 14th, driven by stronger northwest winds following the cold front [40]. The altitude of the dust's outward transmission fell to about 1 km.

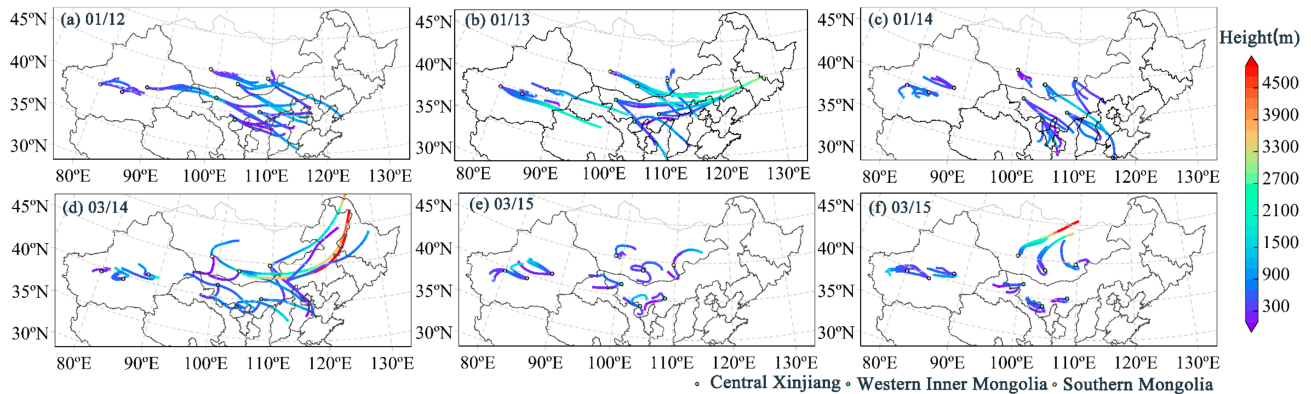


Figure 7. Forward trajectories of dust source areas in the 1.12 and 3.15 events.

On 14 March, a violent Mongolian cyclone blew strong gusts of 7 or 8 and created a large amount of dust in southern Mongolia [18,61]. East winds carried this dust to Northwest and Northeast China, reaching heights of more than 5 km. One part of the dust in western Inner Mongolia only affected locals, while another part was transported to northern China at a height of about 1 km. According to the trajectory of the air mass, the dust raised in southern Mongolia on the 15th and 16th would no longer be transported to China. Dust was also insignificant for outward transportation in central Xinjiang and western Inner Mongolia. This conclusion is supported by satellite images that show intense dust concentrations, primarily in western Inner Mongolia. As a result, the dust that covered the downstream cities during the 3.15 event was primarily caused by dust transported southward from southern Mongolia.

Because PM_{10} concentrations can represent the status of near-surface dust during dust weather, potential sources of PM_{10} can also be considered potential sources of near-surface dust. The 3D-CWT method was used to examine potential dust sources in six representative cities (Figure 8) in order to show more detailed input pathways of near-surface dust in downstream towns.

Jilin was exposed to local dust within 500 m of the ground in both dust events, as shown in Figure 8. Meanwhile, dust from 500–1500 m and 500–3000 m above sea level was delivered to Jilin from southern Mongolia. The dust in Hebei originated primarily in southern Mongolia and central Inner Mongolia, with an incoming height of 1500–3000 m. Furthermore, dust was backflowing from the east and south within 500 m. Shaanxi experienced dust transport not only from western Inner Mongolia at 0–1500 m in the 1.12 event, but also from southern Mongolia at 500–1500 m in the 3.15 event. Shaanxi, like Hebei, was affected by the return flow of dust at 500–1500 m. The dust in Gansu was caused by local dust as well as high-altitude (1500–3000 m) dust from central Xinjiang.

Even though they are farther away from the dust sources in Northwest China, the southern cities are not free from the East Asian dust. According to CWT, dust blowback from the northeast can impact Zhejiang within 500 m, and dust from the northwest can impact Zhejiang at heights ranging from 500 m to 3000 m. When combined with the previous analysis of the dust source's outflow path, it is clear that the dust returning from the northeast via the Yellow Sea would be from southern Mongolia. Hunan's dust came from two directions as well. One ranges from 0 to 1500 m in the northeast and the other from 1500–3000 m in the northwest. According to Hunan's forward trajectory, the incoming dust from the northeast should be a mix of dust from southern Mongolia and western Inner Mongolia. The elevated dust in the northwest is likely to be from central Xinjiang.

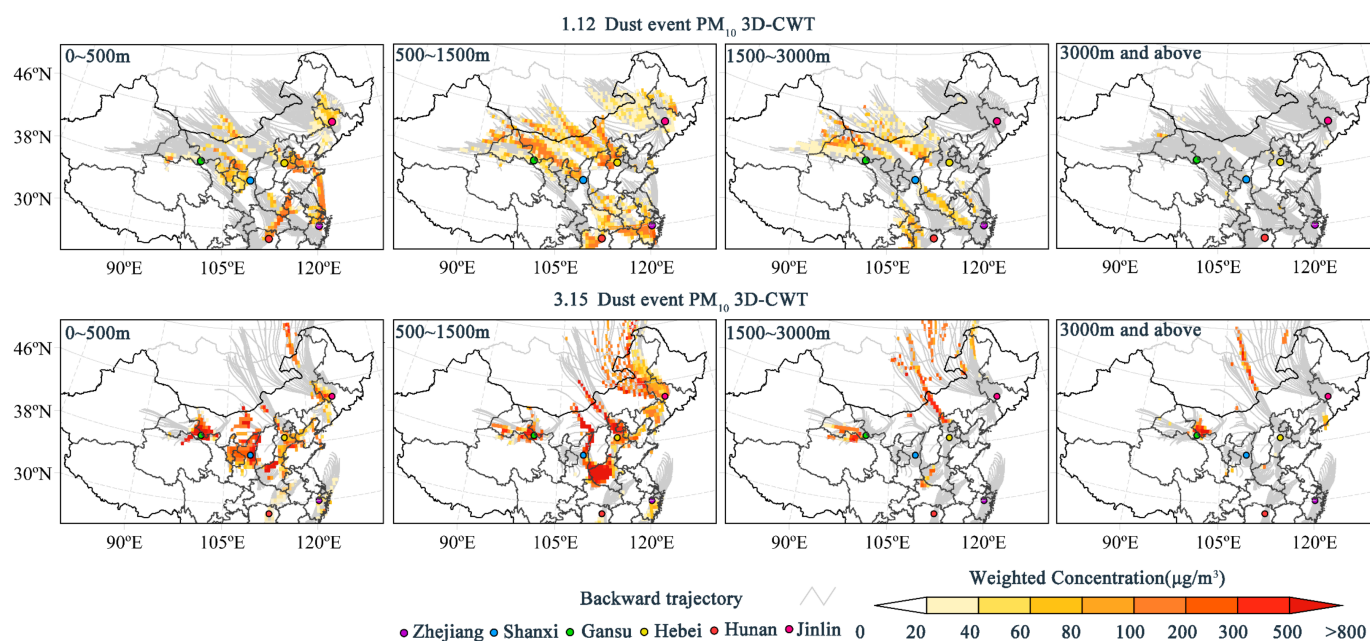


Figure 8. PM₁₀ 3D-CWT results for typical cities in the 1.12 and 3.15 events.

Based on the forward trajectory of sands and 3D-CWT analysis of urban PM₁₀, the dust in the 1.12 event originated primarily in southern Mongolia and western Inner Mongolia. However, the dust affecting downstream cities in the 3.15 event originated more in southern Mongolia. The dust transport path from southern Mongolia can be summarized as two paths. After passing through central Inner Mongolia, the dust moved eastward and reached the northern part of North China and the northwestern part of Northeast China. The other mode of transport is southeastward: dust moved southward through central Inner Mongolia and southeast of Northwest China, then continued south. Dust from western Inner Mongolia traveled eastward, affecting southern North China, and a southeastward path continued southward through southeastern Northwest China. The dust in central Xinjiang is mostly gathered locally due to topography; only dust above 1500 m can be lifted eastward to Gansu and possibly settle in southwest China. In downstream cities, the near-surface dust ranged primarily from 0 to 3000 m. Dust at 500–1500 m height contributed the most to the urban near-surface among the four height layers studied in the paper. Most cities were affected by the returning flow of dust. The eastern coast of China was extremely vulnerable to the return flow of dust from southern Mongolia. Southern cities such as Hunan and Zhejiang, which are far from the dust source, were also affected.

3.3. Impact on Urban Air Quality

In the final section of the study, we analyze changes in particulate matter concentrations and ozone pollution levels in typical cities during the dust period using air pollutant data from ground stations. The data in Figures 3 and 9 show that PM₁₀ and PM_{2.5} concentrations at all sites increase to varying degrees with the development of dust activities. The daily average PM₁₀ and PM_{2.5} levels at the sand source stations in the 3.15 event are 730 µg/m³ and 166 µg/m³, respectively, which are significantly higher than those in the 1.12 event (216 µg/m³ and 59 µg/m³, respectively).

However, particulate matter pollution in downstream cities exhibited distinct characteristics. Particulate matter concentration rose slowly during the 1.12 dust event, followed by a slow decline, whereas it rose and fell at a faster rate during the 3.15 dust event. PM₁₀ pollution exceeded the national secondary pollutant concentration standard (150 µg/m³) in Beijing, Zhejiang, Hunan, Shaanxi, and Henan during the 1.12 dust event. However, Hunan and Zhejiang's PM₁₀ concentrations did not exceed the limit during the 3.15 event. Similarly, the Hunan and Zhejiang sites exceeded the national secondary standard for PM_{2.5}

(75 $\mu\text{g}/\text{m}^3$) in the 1.12 event but not in the 3.15 event. PM pollution was worse in southern cities such as Zhejiang and Hunan during the 1.12 event than it was during the 3.15 event. This is likely due to the 1.12 event's lower altitude. Lower dust concentrations can settle to the ground significantly faster, influencing surface particulate concentrations.

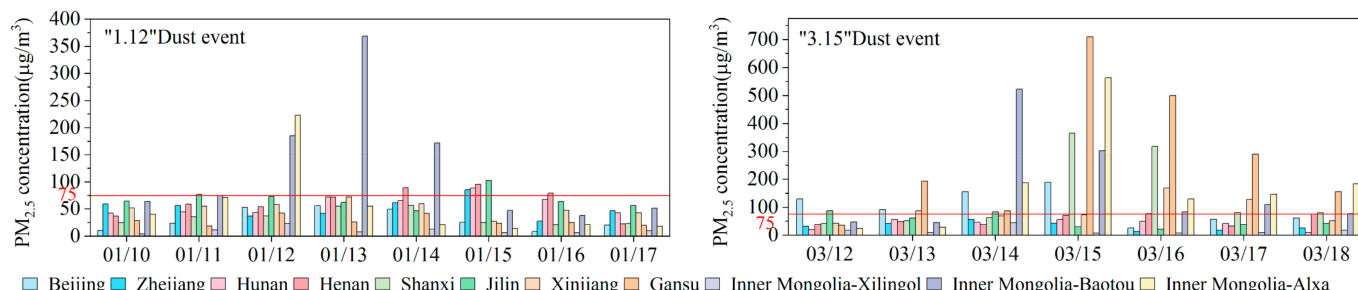


Figure 9. Daily average $\text{PM}_{2.5}$ values at ground stations during the 1.12 and 3.15 events.

Tropospheric ozone is the second most significant urban air pollutant at the moment in China [62]. Many countries, including China, express ozone pollution levels using the daily maximum 8 h sliding average. To investigate the variations in urban ozone pollution during these two dust events, the daily change rates of the daily maximum 8 h sliding average on the high PM_{10} day were calculated. If the site shows only one day of increased PM_{10} concentration during the dust period, that day is designated as the high PM_{10} day. If the site shows more than one day of an increase in PM_{10} value, the first two days of the PM_{10} daily average value are taken in descending order. Data from Tables 1 and 2 show that on dust days, most stations have lower ozone pollution levels. Reduced ozone pollution levels were found in 77% of the sand source stations and 63% of the downstream cities. However, some cities have experienced increased ozone pollution, including Beijing, Zhejiang, Hunan, Henan, and Baotou in eastern Inner Mongolia. Surprisingly, no clear relationship appears to exist between ozone pollution levels and PM_{10} concentrations in either event. Many sites, including Beijing, Shaanxi, and Baotou, showed significantly different ozone pollution variations at similar PM_{10} concentrations.

As mentioned in the literature review, many factors influence the variation of ozone concentration [26], including meteorological conditions [63,64], changes in the concentration of ozone precursors [65], and aerosols that affect photochemical reactions [27]. Several studies have found that dust can affect ozone production and depletion rates by increasing atmospheric extinction [66]. The combination of Gobi dust and anthropogenic pollutants in South-Central China has the potential to stabilize the planetary boundary layer and accelerate ozone formation [67]. Furthermore, during dust events, the violent vertical motion of airflow may result in stratospheric ozone intrusion [68]. Previous research and the data presented in this section both indicate that the patterns and causes of urban ozone changes during dusty weather are complex. Investigating the mechanism of interaction between dust aerosols and ozone will benefit the synergistic effect.

Table 1. Variation of ozone pollution levels in downstream city sites during the 1.12 and 3.15 events.

Stations	High PM_{10} Day	PM_{10} Daily Average ($\mu\text{g}/\text{m}^3$)	Daily Change Rates of the Ozone Pollution Level
Beijing	1.12	155	−60%
	1.13	163	156%
	3.15	1524	86%
	3.17	294	−51%
Zhejiang	1.14	153	−14%
	1.15	197	27%
	3.14	116	20%

Table 1. Cont.

Stations	High PM ₁₀ Day	PM ₁₀ Daily Average (µg/m ³)	Daily Change Rates of the Ozone Pollution Level
Hunan	1.15	156	−17%
	1.16	206	−47%
	3.16	130	61%
Henan	1.15	302	−59%
	1.16	198	41%
	3.15	368	−2%
	3.16	517	−15%
Shaanxi	1.13	216	−23%
	1.14	353	27%
	3.15	2511	−7%
	3.16	1955	−51%
Jinlin	1.15	103	6%
	3.15	339	−23%

Table 2. Variation of ozone pollution levels in sand source sites during the 1.12 and 3.15 events.

Stations	High PM ₁₀ Day	PM ₁₀ Daily Average (µg/m ³)	Daily Change Rates of the Ozone Pollution Level
Xinjiang	1.16	315	−1%
	1.17	232	−20%
	3.16	923	−10%
	3.17	710	−7%
Gansu	1.13	96	−3%
	1.15	32	−7%
	3.15	2484	−21%
	3.16	2731	−9%
Xinlingol	1.12	80	−7%
	3.14	878	46%
Baotou	1.13	1205	−25%
	1.14	774	64%
	3.14	744	−7%
	3.15	664	−22%
Alxa	1.12	1406	2%
	1.13	326	0%
	3.15	3191	−28%
	3.17	1251	−37%

4. Conclusions

The 1.12 event was the first dust event of 2021, occurring one month earlier than usual. The 3.15 dust storm was the most powerful in the previous decade. A goal of this study was to investigate the spatial-temporal distribution and transport of two specific dust events, along with a careful exploration of their effects on air quality in sand source and non-sand-source cities.

- (1) Both events had comparable impact areas, according to satellite, ground, and reanalysis data, including Northeast, North, Northwest, Central-South, and East China. China's Northwest, North, and Northeast regions experienced intense dust storms during the 3.15 event. The vertical distribution of dust was 0–5 km in 1.12 event and 0–10 km in 3.15 event.

- (2) The dust from the 1.12 event originated in western Inner Mongolia and southern Mongolia, whereas the dust from the 3.15 event was predominantly from southern Mongolia, according to the HYSPLIT model and the 3D-CWT model. Both of these dust sources have eastward and southeastward transport paths.
- (3) Near-surface dust was primarily transmitted from 0–3 km in downstream cities. The contribution of dust was greater in the 500–1500 m height range. The returning flow of dust impacted the majority of cities. The eastern coast of China was extremely vulnerable to the return flow of dust from southern Mongolia. Southern cities such as Hunan and Zhejiang, which are far from the dust source, were also vulnerable to East Asian dust. Desertification control in China requires increased international cooperation with Mongolia.
- (4) These two dust processes caused severe particulate pollution at the sand source and downstream cities. The particle pollution in 3.15 was worse than in 1.12 in northern China but less severe than in 1.12 in southern China. The rising and falling rates of particulate concentrations in downstream cities were slower in the 1.12 dust event than in the 3.15 dust event. Dust events with low dust heights and dust backflow should be given special consideration in urban dust pollution forecasting and warning. During these two dust events, most stations showed decreasing ozone pollution, but some showed elevated ozone pollution. The complex variation of ozone concentrations during dust weather warrants further investigation.
- (5) Overall, this study enhances our understanding of the formation and development of dust events in East Asia and explores the dust pollution of non-sand-source cities in China. Furthermore, the innovative use of the 3D-CWT model highlights the significance of dust height on downstream urban particle pollution. This distance functions as a point of reference for the early warning and regional joint prevention and control of dust pollution. Due to a lack of sand data, this paper only uses the HYSPLIT model's air mass trajectories to simulate the dust path, without taking the sand's surface conditions into account. Future research will combine remote sensing data with numerical models that integrate various elements, such as WRF-chem and CMAQ, to investigate the mechanisms of dust aerosols' influence on urban air quality in greater depth.

Author Contributions: Q.Y. designed the experiment and wrote the manuscript. X.Z. helped to improve the manuscript. All authors have read and agreed to the published version of the manuscript.

Funding: This research received no external funding.

Institutional Review Board Statement: Not applicable.

Informed Consent Statement: Not applicable.

Data Availability Statement: Not applicable.

Acknowledgments: The authors thank the National Natural Science Foundation of China's "Western China Environmental and Ecological Science Data Center" (<http://westdc.westgis.ac.cn>, accessed on 10 January 2023) for providing the sand type data and the Graduate Research Innovation Program from Tianjin University of Science and Technology for their support.

Conflicts of Interest: The authors declare no conflict of interest.

References

1. Dubovik, O.; Holben, B.; Eck, T.F.; Smirnov, A.; Kaufman, Y.J.; King, M.D.; Tanre, D.; Slutsker, I. Variability of absorption and optical properties of key aerosol types observed in worldwide locations. *J. Atmos. Sci.* **2002**, *59*, 590–608. [[CrossRef](#)]
2. Yu, H.; Kaufman, Y.J.; Chin, M.; Feingold, G.; Remer, L.A.; Anderson, T.L.; Balkanski, Y.; Bellouin, N.; Boucher, O.; Christopher, S.; et al. A review of measurement-based assessments of the aerosol direct radiative effect and forcing. *Atmos. Chem. Phys.* **2006**, *6*, 613–666. [[CrossRef](#)]
3. Alonso-Montesinos, J.; Barbero, J.; Lopez, G.; Ballestrin, J.; Polo, J.; Marzo, A.; Batlles, F.J. The influence of Sahara dust particles in the direct normal irradiance estimation through a total sky camera. In Proceedings of the 11th ISES Eurosun 2016 Conference, Palma de Mallorca, Spain, 11–14 October 2016; pp. 1413–1421.

4. Ramanathan, V.; Crutzen, P.J.; Lelieveld, J.; Mitra, A.P.; Althausen, D.; Anderson, J.; Andreae, M.O.; Cantrell, W.; Cass, G.R.; Chung, C.E.; et al. Indian Ocean Experiment: An integrated analysis of the climate forcing and effects of the great Indo-Asian haze. *J. Geophys. Res. Atmos.* **2001**, *106*, 28371–28398. [[CrossRef](#)]
5. Andreae, M.O.; Rosenfeld, D. Aerosol-cloud-precipitation interactions. Part 1. The nature and sources of cloud-active aerosols. *Earth-Sci. Rev.* **2008**, *89*, 13–41. [[CrossRef](#)]
6. Oh, S.H.; Park, K.; Park, M.; Song, M.Y.K.; Jang, K.S.; Schauer, J.J.; Bae, G.N.; Bae, M.S. Comparison of the sources and oxidative potential of PM_{2.5} during winter time in large cities in China and South Korea. *Sci. Total Environ.* **2023**, *859*, 160369. [[CrossRef](#)]
7. Bin, C.; Song, Z.H.; Huang, J.P.; Zhang, P.; Hu, X.Q.; Zhang, X.Y.; Guan, X.D.; Ge, J.M.; Zhou, X.Z. Estimation of Atmospheric PM₁₀ Concentration in China Using an Interpretable Deep Learning Model and Top-of-the-Atmosphere Reflectance Data from China's New Generation Geostationary Meteorological Satellite, FY-4A. *J. Geophys. Res. Atmos.* **2022**, *127*, e2021JD036393. [[CrossRef](#)]
8. Das, S.; Prospero, J.M.; Chellam, S. Quantifying international and interstate contributions to primary ambient PM_{2.5} and PM₁₀ in a complex metropolitan atmosphere. *Atmos. Environ.* **2023**, *292*, 119415. [[CrossRef](#)]
9. Panunzi, S.; Marchetti, P.; Stafoggia, M.; Badaloni, C.; Caranci, N.; de Hoogh, K.; Rossi, P.G.; Guarda, L.; Locatelli, F.; Ottone, M.; et al. Residential exposure to air pollution and adverse respiratory and allergic outcomes in children and adolescents living in a chipboard industrial area of Northern Italy. *Sci. Total Environ.* **2023**, *864*, 161070. [[CrossRef](#)]
10. Zhang, L.; Li, S.; Wang, B.; Liu, C.; He, L.; Shan, X.B.; Zhang, K.; Luo, B. Effects of Dust Event Days on Influenza: Evidence from Arid Environments in Lanzhou. *Aerosol Air Qual. Res.* **2022**, *22*, 220282. [[CrossRef](#)]
11. Yang, Y.; Zeng, L.Y.; Wang, H.L.; Wang, P.Y.; Liao, H. Dust pollution in China affected by different spatial and temporal types of El Niño. *Atmos. Chem. Phys.* **2022**, *22*, 14489–14502. [[CrossRef](#)]
12. Yao, X.F.; Ge, B.Z.; Li, A.B.; Chen, G.J.; Fan, F.; Xu, D.H.; Wang, Y.G.; Tang, X.; Kong, L.; Wang, Z.F. Spatio-temporal variation of PM_{2.5} pollution in Xinjiang and its causes: The growing importance in air pollution situation in China. *Front. Environ. Sci.* **2023**, *10*, 1051610. [[CrossRef](#)]
13. Patel, K.; Chaurasia, M.; Rao, K.S. Urban dust pollution tolerance indices of selected plant species for development of urban greenery in Delhi. *Environ. Monit. Assess.* **2023**, *195*, 16. [[CrossRef](#)] [[PubMed](#)]
14. Jiang, Z.C.; Lian, Y.Q.; Qin, X.Q. Rocky desertification in Southwest China: Impacts, causes, and restoration. *Earth-Sci. Rev.* **2014**, *132*, 1–12. [[CrossRef](#)]
15. Aili, A.; Xu, H.L.; Kasim, T.; Abulikemu, A. Origin and Transport Pathway of Dust Storm and Its Contribution to Particulate Air Pollution in Northeast Edge of Taklimakan Desert, China. *Atmosphere* **2021**, *12*, 113. [[CrossRef](#)]
16. Takemi, T.; Seino, N. Dust storms and cyclone tracks over the arid regions in east Asia in spring. *J. Geophys. Res. Atmos.* **2005**, *110*, D18S11. [[CrossRef](#)]
17. Li, J.D.; Hao, X.; Liao, H.; Yue, X.; Li, H.; Long, X.; Li, N. Predominant Type of Dust Storms That Influences Air Quality Over Northern China and Future Projections. *Earths Future* **2022**, *10*, e2022EF002649. [[CrossRef](#)]
18. Zhang, T.L.; Zheng, M.; Sun, X.G.; Chen, H.H.; Wang, Y.T.; Fan, X.H.; Pan, Y.B.; Quan, J.N.; Liu, J.Y.; Wang, Y.A.; et al. Environmental impacts of three Asian dust events in the northern China and the northwestern Pacific in spring 2021. *Sci. Total Environ.* **2023**, *859*, 160230. [[CrossRef](#)]
19. Yang, L.L.; Zhang, S.W.; Huang, Z.W.; Yang, Y.P.; Wang, L.N.; Han, W.Y.; Li, X.Y. Characteristics of Dust Events in China from 2015 to 2020. *Atmosphere* **2021**, *12*, 952. [[CrossRef](#)]
20. Liu, Y.; Yi, B. Aerosols over East and South Asia: Type Identification, Optical Properties, and Implications for Radiative Forcing. *Remote Sens.* **2022**, *14*, 2058. [[CrossRef](#)]
21. Liu, C.T.; Xin, Y.Y.; Zhang, C.L.; Liu, J.F.; Liu, P.F.; He, X.W.; Mu, Y.J. Ambient volatile organic compounds in urban and industrial regions in Beijing: Characteristics, source apportionment, secondary transformation and health risk assessment. *Sci. Total Environ.* **2023**, *855*, 158873. [[CrossRef](#)]
22. Wei, J.; Li, Z.Q.; Li, K.; Dickerson, R.R.; Pinker, R.T.; Wang, J.; Liu, X.; Sun, L.; Xue, W.H.; Cribb, M. Full-coverage mapping and spatiotemporal variations of ground-level ozone (O₃) pollution from 2013 to 2020 across China. *Remote Sens. Environ.* **2022**, *270*, 112775. [[CrossRef](#)]
23. Chen, Y.L.; Li, H.C.; Karimian, H.; Li, M.M.; Fan, Q.; Xu, Z.G. Spatio-temporal variation of ozone pollution risk and its influencing factors in China based on Geodetector and Geospatial models. *Chemosphere* **2022**, *302*, 134843. [[CrossRef](#)] [[PubMed](#)]
24. Ding, S.; Jiang, X.T.; Wu, C.H. Contrasting Near-Surface Ozone Pollution in Wet and Dry Year over China. *Int. J. Environ. Res. Public Health* **2023**, *20*, 998. [[CrossRef](#)]
25. Zhu, X.W.; Wu, J.; Tang, G.Q.; Qiao, L.; Han, T.T.; Yin, X.M.; Liu, X.X.; Li, Z.M.; Xiong, Y.J.; He, D.; et al. Influence of circulation types on temporal and spatial variations of ozone in Beijing. *J. Environ. Sci.* **2023**, *130*, 37–51. [[CrossRef](#)]
26. Zhang, X.X.; Yan, B.; Du, C.J.; Cheng, C.X.; Zhao, H. Quantifying the interactive effects of meteorological, socioeconomic, and pollutant factors on summertime ozone pollution in China during the implementation of two important policies. *Atmos. Pollut. Res.* **2021**, *12*, 101248. [[CrossRef](#)]
27. Gharibzadeh, M.; Bidokhti, A.A.; Alam, K. The interaction of ozone and aerosol in a semi-arid region in the Middle East: Ozone formation and radiative forcing implications. *Atmos. Environ.* **2021**, *245*, 118015. [[CrossRef](#)]

28. Meinander, O.; Dagsson-Waldhauserova, P.; Amosov, P.; Aseyeva, E.; Atkins, C.; Baklanov, A.; Baldo, C.; Barr, S.L.; Barzycka, B.; Benning, L.G.; et al. Newly identified climatically and environmentally significant high-latitude dust sources. *Atmos. Chem. Phys.* **2022**, *22*, 11889–11930. [[CrossRef](#)]
29. Han, J.; Dai, H.; Gu, Z.L. Sandstorms and desertification in Mongolia, an example of future climate events: A review. *Environ. Chem. Lett.* **2021**, *19*, 4063–4073. [[CrossRef](#)] [[PubMed](#)]
30. Liu, S.; Xing, J.; Sahu, S.K.; Liu, X.; Liu, S.; Jiang, Y.; Zhang, H.; Li, S.; Ding, D.; Chang, X.; et al. Wind-blown dust and its impacts on particulate matter pollution in Northern China: Current and future scenarios. *Environ. Res. Lett.* **2021**, *16*, 114041. [[CrossRef](#)]
31. He, Y.; Yi, F.; Yin, Z.; Liu, F.; Yi, Y.; Zhou, J. Mega Asian dust event over China on 27–31 March 2021 observed with space-borne instruments and ground-based polarization lidar. *Atmos. Environ.* **2022**, *285*, 119238. [[CrossRef](#)]
32. Filonchik, M.; Peterson, M. Development, progression, and impact on urban air quality of the dust storm in Asia in March 15–18, 2021. *Urban Clim.* **2022**, *41*, 101080. [[CrossRef](#)]
33. Gui, K.; Yao, W.; Che, H.; An, L.; Zheng, Y.; Li, L.; Zhao, H.; Zhang, L.; Zhong, J.; Wang, Y.; et al. Record-breaking dust loading during two mega dust storm events over northern China in March 2021: Aerosol optical and radiative properties and meteorological drivers. *Atmos. Chem. Phys.* **2022**, *22*, 7905–7932. [[CrossRef](#)]
34. Liang, P.; Chen, B.; Yang, X.; Liu, Q.; Li, A.; Mackenzie, L.; Zhang, D. Revealing the dust transport processes of the 2021 mega dust storm event in northern China. *Sci. Bull.* **2022**, *67*, 21–24. [[CrossRef](#)] [[PubMed](#)]
35. Jin, J.; Pang, M.; Segers, A.; Han, W.; Fang, L.; Li, B.; Feng, H.; Lin, H.X.; Liao, H. Inverse modeling of the 2021 spring super dust storms in East Asia. *Atmos. Chem. Phys.* **2022**, *22*, 6393–6410. [[CrossRef](#)]
36. Sun, X.G.; Fan, X.H.; Zhang, T.L.; Wang, Y.A.; Wang, Y.T.; Lyu, D.; Zheng, M. Tempo-Spatial Distributions and Transport Characteristics of Two Dust Events over Northern China in March 2021. *Remote Sens.* **2022**, *14*, 5967. [[CrossRef](#)]
37. Wang, X.M.; Hua, T.; Che, H.Z. Temporal variation of dust aerosol pollution in northern China. *Arab. J. Geosci.* **2020**, *13*, 108. [[CrossRef](#)]
38. Zou, X.K.K.; Zhai, P.M.M. Relationship between vegetation coverage and spring dust storms over northern China. *J. Geophys. Res. Atmos.* **2004**, *109*, 9. [[CrossRef](#)]
39. Wang, F.; Wang, M.Q.; Kong, Y.F.; Zhang, H.P.; Ru, X.T.; Song, H.Q. Spatial and Temporal Variations in Spring Dust Concentrations from 2000 to 2020 in China: Simulations with WRF-Chem. *Remote Sens.* **2022**, *14*, 13. [[CrossRef](#)]
40. Jiang, Q.; Gui, H.; Xu, R. Analysis of January 2020 Atmospheric Circulation and Weather. *Meteorol. Mon.* **2021**, *47*, 510–516.
41. Guan, T.; Zhang, T.; Li, X. Analysis of the March 2021 Atmospheric Circulation and Weather. *Meteorol. Mon.* **2021**, *47*, 767–772.
42. Garane, K.; Chan, K.L.; Koukouli, M.E.; Loyola, D.; Balis, D. TROPOMI/S5P Total Column Water Vapor validation against AERONET ground-based measurements. *Atmos. Meas. Tech.* **2023**, *16*, 57–74. [[CrossRef](#)]
43. Zhang, L.J.; Ding, S.J.; Qian, W.M.; Zhao, A.M.; Zhao, S.M.; Yang, Y.; Weng, G.Q.; Tao, M.H.; Chen, H.; Zhao, S.H.; et al. The Impact of Long-Range Transport of Biomass Burning Emissions in Southeast Asia on Southern China. *Atmosphere* **2022**, *13*, 1029. [[CrossRef](#)]
44. Torres, O.; Jethva, H.; Ahn, C.; Jaross, G.; Loyola, D.G. TROPOMI aerosol products: Evaluation and observations of synoptic-scale carbonaceous aerosol plumes during 2018–2020. *Atmos. Meas. Tech.* **2020**, *13*, 6789–6806. [[CrossRef](#)]
45. Chen, B.; Huang, J.; Minnis, P.; Hu, Y.; Yi, Y.; Liu, Z.; Zhang, D.; Wang, X. Detection of dust aerosol by combining CALIPSO active lidar and passive IIR measurements. *Atmos. Chem. Phys.* **2010**, *10*, 4241–4251. [[CrossRef](#)]
46. Chen, B.; Song, Z.H.; Pan, F.; Huang, Y. Obtaining vertical distribution of PM_{2.5} from CALIOP data and machine learning algorithms. *Sci. Total Environ.* **2022**, *805*, 150338. [[CrossRef](#)]
47. Bucharad, V.; Randles, C.A.; da Silva, A.M.; Darmanov, A.; Colarco, P.R.; Govindaraju, R.; Ferrare, R.; Hair, J.; Beyersdorf, A.J.; Ziemba, L.D.; et al. The MERRA-2 Aerosol Reanalysis, 1980 Onward. Part II: Evaluation and Case Studies. *J. Clim.* **2017**, *30*, 6851–6872. [[CrossRef](#)] [[PubMed](#)]
48. Stein, A.F.; Draxler, R.R.; Rolph, G.D.; Stunder, B.J.B.; Cohen, M.D.; Ngan, F. NOAA’s Hysplit Atmospheric Transport and Dispersion Modeling System. *Bull. Am. Meteorol. Soc.* **2015**, *96*, 2059–2077. [[CrossRef](#)]
49. Ge, C.D.; Liu, J.; Cheng, X.G.; Fang, K.Y.; Chen, Z.X.; Chen, Z.B.; Hu, J.; Jiang, D.S.; Shen, L.J.; Yang, M.M. Impact of regional transport on high ozone episodes in southeast coastal regions of China. *Atmos. Pollut. Res.* **2022**, *13*, 101497. [[CrossRef](#)]
50. Dong, L.; Chen, B.; Huang, Y.; Song, Z.H.; Yang, T.T. Analysis on the Characteristics of Air Pollution in China during the COVID-19 Outbreak. *Atmosphere* **2021**, *12*, 205. [[CrossRef](#)]
51. Zhan, Y.Z.H.; Xie, M.; Gao, D.; Wang, T.J.; Zhang, M.; An, F.X. Characterization and source analysis of water-soluble inorganic ionic species in PM_{2.5} during a wintertime particle pollution episode in Nanjing, China. *Atmos. Res.* **2021**, *262*, 105769. [[CrossRef](#)]
52. Bai, D.P.; Wang, H.L.; Cheng, M.T.; Gao, W.K.; Yang, Y.; Huang, W.; Ma, K.J.; Zhang, Y.; Zhang, R.J.; Zou, J.N.; et al. Source apportionment of PM_{2.5} and its optical properties during a regional haze episode over north China plain. *Atmos. Pollut. Res.* **2020**, *12*, 89–99. [[CrossRef](#)]
53. Kong, L.W.; Tan, Q.W.; Feng, M.; Qu, Y.; An, J.L.; Liu, X.G.; Cheng, N.L.; Deng, Y.J.; Zhai, R.X.; Wang, Z. Investigating the characteristics and source analyses of PM_{2.5} seasonal variations in Chengdu, Southwest China. *Chemosphere* **2020**, *243*, 125267. [[CrossRef](#)] [[PubMed](#)]
54. Nguyen, T.N.T.; Vuong, Q.T.; Lee, S.J.; Xiao, H.; Choi, S.D. Identification of source areas of polycyclic aromatic hydrocarbons in Ulsan, South Korea, using hybrid receptor models and the conditional bivariate probability function. *Environ. Sci. Process. Impacts* **2022**, *24*, 140–151. [[CrossRef](#)] [[PubMed](#)]

55. Dimitriou, K.; Mihalopoulos, N.; Leeson, S.R.; Twigg, M.M. Sources of PM_{2.5}-bound water soluble ions at EMEP's Auchincorth Moss (UK) supersite revealed by 3D-Concentration Weighted Trajectory (CWT) model. *Chemosphere* **2021**, *274*, 129979. [[CrossRef](#)] [[PubMed](#)]
56. Dimitriou, K.; Pikridas, M.; Oikonomou, K.; Sciare, J.; Savvides, C.; Vassiliadou, E.; Mihalopoulos, N. A 3-Dimensional analysis of long-range transported particulate matter to the Eastern Mediterranean: Implication for the chemical components of PM₁ and PM₁₀. *Atmos. Pollut. Res.* **2022**, *13*, 101485. [[CrossRef](#)]
57. Zhao, Y.F.; Wang, Y.Q.; Liang, C.H.; Wang, J.J.; Fang, J.; Zhou, M.X. Study of Mixed Pollution of Haze and Dust in Jinan Based on LiDAR. *Photonics* **2022**, *9*, 144. [[CrossRef](#)]
58. Tsai, F.J.; Yao, W.C.; Lin, M.L. Analysis of Meteorological Conditions on Riverbed Dust Aerosol in Taiwan. *Atmosphere* **2022**, *13*, 106. [[CrossRef](#)]
59. Tong, P.F.; Chen, S.X.; Tang, C.Y. Detecting and Evaluating Dust-Events in North China with Ground Air Quality Data. *Earth Space Sci.* **2022**, *9*, e2021EA001849. [[CrossRef](#)]
60. Wang, N.; Chen, J.; Zhang, Y.Y.; Xu, Y.M.; Cul, J.W. Multi-source remote sensing analysis of the first sand and dust weather in Northern China in 2021. *China Environ. Sci.* **2022**, *42*, 2002–2014. [[CrossRef](#)]
61. Bueh, C.; Zhuge, A.; Xie, Z.; Yong, M.; Purevjav, G. The development of a powerful Mongolian cyclone on 14–15 March 2021: Eddy energy analysis. *Atmos. Ocean. Sci. Lett.* **2022**, *15*, 44–51. [[CrossRef](#)]
62. Lyu, Y.; Ju, Q.R.; Lv, F.M.; Feng, J.L.; Pang, X.B.; Li, X. Spatiotemporal variations of air pollutants and ozone prediction using machine learning algorithms in the Beijing-Tianjin-Hebei region from 2014 to 2021. *Environ. Pollut.* **2022**, *306*, 119420. [[CrossRef](#)] [[PubMed](#)]
63. Gao, J.; Zhu, B.; Xiao, H.; Kang, H.; Hou, X.; Yin, Y.; Zhang, L.; Miao, Q. Diurnal variations and source apportionment of ozone at the summit of Mount Huang, a rural site in Eastern China. *Environ. Pollut.* **2017**, *222*, 513–522. [[CrossRef](#)]
64. Zhang, Y.; Tian, Q.Q.; Wei, X.Y.; Feng, X.Y.; Ma, P.; Hu, W.D.; Xin, J.Y.; Ni, C.J.; Wang, S.G.; Zheng, C.J. Temperature modulation of adverse consequences of ozone exposure on cardiovascular mortality: A study of multiple cities in China. *Atmos. Environ.* **2022**, *288*, 119272. [[CrossRef](#)]
65. Zhao, M.; Zhang, Y.N.; Pei, C.L.; Chen, T.S.; Mu, J.S.; Liu, Y.H.; Wang, Y.J.; Wang, W.X.; Xue, L.K. Worsening ozone air pollution with reduced NO_x and VOCs in the Pearl River Delta region in autumn 2019: Implications for national control policy in China. *J. Environ. Manag.* **2022**, *324*, 116327. [[CrossRef](#)] [[PubMed](#)]
66. Mukherjee, T.; Vinoj, V.; Midya, S.K.; Adhikary, B. Aerosol radiative impact on surface ozone during a heavy dust and biomass burning event over South Asia. *Atmos. Environ.* **2020**, *223*, 117201. [[CrossRef](#)]
67. Wang, Z.L.; Huang, X.; Wang, N.; Xu, J.W.; Ding, A.J. Aerosol-Radiation Interactions of Dust Storm Deteriorate Particle and Ozone Pollution in East China. *J. Geophys. Res. Atmos.* **2020**, *125*, e2020JD033601. [[CrossRef](#)]
68. Yang, Y.; Wang, Z.; Lou, S.; Xue, L.; Lu, J.; Wang, H.; Wang, J.; Ding, A.; Huang, X. Strong ozone intrusions associated with super dust storms in East Asia. *Atmos. Environ.* **2022**, *290*, 119355. [[CrossRef](#)]

Disclaimer/Publisher's Note: The statements, opinions and data contained in all publications are solely those of the individual author(s) and contributor(s) and not of MDPI and/or the editor(s). MDPI and/or the editor(s) disclaim responsibility for any injury to people or property resulting from any ideas, methods, instructions or products referred to in the content.